SPITZER 70 AND 160 μm OBSERVATIONS OF THE COSMOS FIELD

D. T. Frayer[1], D. B. Sanders[2], J. A. Surace[3], H. Aussel[4], M. Salvato[5], E. Le Floc'h[2], M. T. Huynh[1], N. Z. Scoville[5], A. Afonso-Luis[6], B. Bhattacharya[1], P. Capak[3], D. Fadda[1], H. Fu[5], G. Helou[1], O. Ilbert[2], J. S. Kartaltepe[2], A. M. Koekemoer[7], N. Lee[2], E. Murphy[3], M. T. Sargent[8], E. Schinnerer[8], K. Sheth[3], P. L. Shopbell[5], D. L. Shupe[1], and L. Yan[3]

[1] Infrared Processing and Analysis Center, California Institute of Technology 100-22, Pasadena, CA 91125, USA
[2] Institute for Astronomy, 2680 Woodlawn Drive, University of Hawaii, Honolulu, HI 96822, USA
[3] Spitzer Science Center, California Institute of Technology 220-06, Pasadena, CA 91125, USA
[4] CNRS, AIM-Unité Mixte de Recherche CEA-CNRS-Université Paris VII-UMR 7158, F-91191 Gif-sur-Yvette, France
[5] Astronomy Department, California Institute of Technology 105-24, Pasadena, CA 91125, USA
[6] Instituto Astrofísica de Canarias, Via Lactea, 38200 La Laguna, S/C de Tenerife, Spain
[7] Space Telescope Science Institute, 3700 San Martin Drive, Baltimore, MD 21218, USA
[8] Max-Planck-Institut für Astronomie, Königstuhl 17, D-69117 Heidelberg, Germany
Received 2009 February 17; accepted 2009 August 15; published 2009 September 22

ABSTRACT

We present *Spitzer* 70 and 160 μm observations of the COSMOS *Spitzer* survey (S-COSMOS). The data processing techniques are discussed for the publicly released products consisting of images and source catalogs. We present accurate 70 and 160 μm source counts of the COSMOS field and find reasonable agreement with measurements in other fields and with model predictions. The previously reported counts for GOODS-North and the extragalactic First Look Survey are updated with the latest calibration, and counts are measured based on the large area SWIRE survey to constrain the bright source counts. We measure an extragalactic confusion noise level of $\sigma_c = 9.4 \pm 3.3$ mJy ($q = 5$) for the MIPS 160 μm band based on the deep S-COSMOS data and report an updated confusion noise level of $\sigma_c = 0.35 \pm 0.15$ mJy ($q = 5$) for the MIPS 70 μm band.

Key words: galaxies: evolution – galaxies: starburst – infrared: galaxies

Online-only material: machine-readable and VO tables

1. INTRODUCTION

The Cosmic Evolution Survey (COSMOS) is a deep multiwavelength wide area (2 deg^2) program for studying the evolution of galaxies and active galactic nuclei (AGNs; Scoville et al. 2007). The COSMOS *Spitzer* (S-COSMOS) survey is composed of the Infrared Array Camera (IRAC; 3.6–8 μm) and the Multiband Imaging Photometer for *Spitzer* (MIPS; 24, 70, and 160 μm) data (Sanders et al. 2007). This paper presents the far-infrared (FIR) 70 and 160 μm MIPS observations of the field. Although the mid-infrared (MIR) 24 μm array is more sensitive to the detection of distant galaxies than the MIPS-Germanium (MIPS-Ge) 70 and 160 μm detectors, the 24 μm data are biased toward warm AGNs and are affected by broad mid-infrared PAH emission and silicate absorption features redshifted into the band. The strong MIR spectral features along with the large variations of the FIR/MIR continuum ratios (e.g., Dale et al. 2005) yield highly uncertain bolometric corrections. The long-wavelength 70 and 160 μm observations directly measure the FIR peak of the spectral energy distributions (SEDs) for redshifts $z \lesssim 1.5$ and are key for constraining the total infrared luminosities and star formation rates of galaxies within the COSMOS field. The MIPS 70 and 160 μm data provide an important piece of the puzzle in the quest of understanding galaxy evolution.

The goal of the data paper is to document the data products to facilitate the ongoing research of the COSMOS field. The data products and a description of the observations and data reduction are provided as part of the large public repository of multiwavelength data for the COSMOS field (*Hubble Space Telescope* Advanced Camera for Surveys (ACS), Koekemoer et al. 2007; radio, Schinnerer et al. 2007; X-ray, Hasinger et al.

2007; and optical and near-infrared, Capak et al. 2007). We present two scientific results here: (1) the 70 and 160 μm source counts, and (2) the measurement of the confusion noise for the MIPS 160 μm band.

2. OBSERVATIONS

The MIPS S-COSMOS observations were carried out in four campaigns from 2006 January to 2008 January (Table 1). The project (*Spitzer* programs 20070 and 30143) represents over 450 hr of MIPS observations. All observations were taken using the scan mapping mode during nominal "Cold" MIPS campaigns (telescope temperatures low enough to yield good quality 160 μm data). The initial observations taken in 2006 Cycle-2 are described by Sanders et al. (2007). The Cycle-2 observations were comprised of a shallow wide area (1.75 deg ×1.97 deg) survey to quantify the level of cirrus within the field and a small (0.5 deg ×0.33 deg) deep "test" field. After the successful completion of the Cycle-2 program, deep observations over the entire COSMOS field were carried out in Cycle-3 (depth of about 2800 s, 1350 s, and 270 s in the MIPS 24, 70, and 160 μm bands, respectively).

The Cycle-3 astronomical observational requests (AORs) were optimized specifically for the MIPS-Ge bands, without compromising the 24 μm data. In contrast, some early MIPS programs of other groups were designed for the 24 μm band at the expense of the MIPS-Ge bands. The forward and return scan legs were offset by 148″, which provides sufficient overlap for the 70 μm array. Cross-scan dither offsets of ±0, 42, 83″ and in-scan dither offsets of ±0, 18″ were used between multiple maps to account for the unusable parts of the MIPS-Ge arrays and the unobserved central row of the 160 μm footprint. The values
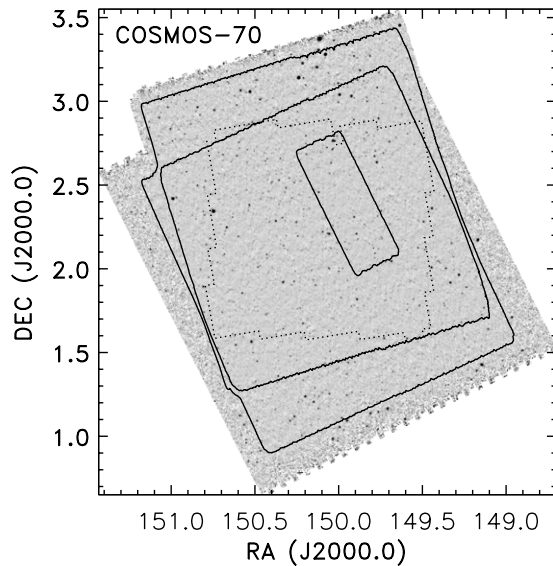
Figure 1. S-COSMOS 70 μm image shown on a logarithmic gray scale. The solid lines show contours representing coverages of 50, 100, and 250 observations. The central rectangle (highest coverage $\geqslant$ 250) shows the Cycle-2 test field, and the dotted line shows the extent of the *HST* ACS field.
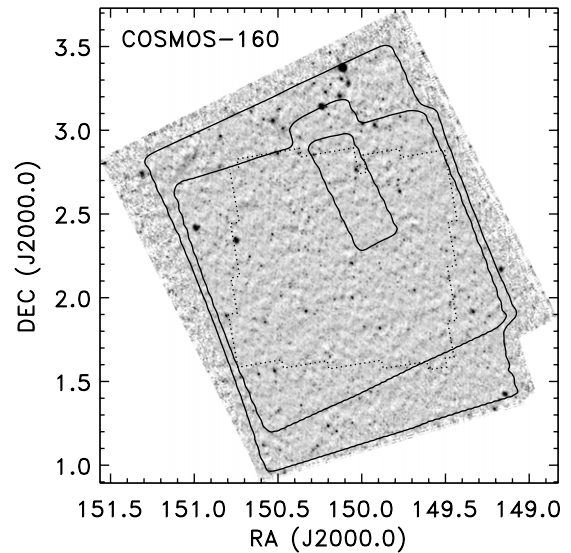
Figure 2. S-COSMOS 160 μm image shown on a logarithmic gray scale. The solid lines show contours representing a coverage of 10, 20, and 50 observations. The deep central contour shows the Cycle-2 test field, and the dotted line shows the extent of the *HST* ACS field.

Table 1
Spitzer COSMOS Observations with MIPS

Epoch	Dates	Campaign	AORs
Cycle-2	2006 Jan 6–9	MIPS006300	21
Cycle-3a	2007 Jan 1–13	MIPS010800	70
Cycle-3b	2007 May 18–28	MIPS011900	61
Cycle-3c	2008 Jan 6–7	MIPS013500	5

Note. *Spitzer* programs 20070 and 30143.

of the cross-scan dithers were also chosen to avoid the overlap of 24 μm readouts between consecutive maps. We carried out both forward and reverse scan maps to help characterize the long-term transients of the MIPS-Ge detectors.

The majority of the data were taken in a slow scan mode. At the slow scan speed ($2\farcs6$ s^{-1}), each AOR consisted of four scan legs of 1.5 deg. Each AOR mapped 1.5 deg $\times$ 592$''$, and 10 AORs were used to map the field once. In total, 13 slow maps (29.5 hr per map) were carried out in Cycle-3, along with one map at the medium scan rate (12.5 hr) to complete the awarded time. Five AORs were lost due to satellite downlink issues in the second epoch of Cycle-3 and were reobserved in early 2008 (Cycle-3c, Table 1).

The scan direction of MIPS is determined by the date of observation, and the observations were carried out on the days that minimized the zodiacal light. Since the field is near the ecliptic plane, the zodiacal background contributes significantly to the total noise budget for the MIPS 24 and 70 μm bands. The zodiacal light is not significant at 160 μm. The galactic cirrus level is low in the direction of the COSMOS field (Sanders et al. 2007) and is not the dominant source of confusion noise within the MIPS-Ge bands. Figures 1 and 2 show the final MIPS 70 and 160 μm images, combining all epochs (Table 1). Since the 70 μm and 160 μm arrays are on the opposite side of the MIPS field of view, the overscan regions yield slightly nonsymmetric coverage. For both Cycle-3a and Cycle-3b, the entire ACS field was observed, and the MIPS overscan regions provide coverage for the IRAC data outside of the ACS field.

3. DATA REDUCTION

The raw MIPS-Germanium 70 and 160 μm (MIPS-Ge) data were downloaded from the Spitzer Science Center (SSC) archive and were reduced using the Germanium Reprocessing Tools (GeRT, version 20060415) and additional specialized scripts developed for processing the MIPS-Ge survey data. The GeRT uses an offline version of the SSC pipeline to produce the basic calibrated data products (BCDs). The basic MIPS-Ge processing steps are discussed by Gordon et al. (2005) and are within the GeRT documentation. The processing for S-COSMOS made use of lessons learned from the processing of the extragalactic First Look Survey (xFLS; Frayer et al. 2006a) and the deep GOODS-North observations (Frayer et al. 2006b). Additional processing enhancements were derived here using the S-COSMOS data.

The main processing steps were carried out in the following order: (1) calculation of the data ramp slope, (2) stimulator-flash interpolation, (3) improved stimulator-flash response solution, (4) calibration of the slope image to yield the BCD product, (5) enhanced filtering of the BCD product, (6) data coaddition, (7) identification of bright sources, (8) masking bright sources and recalculation of the filtering corrections, (9) final data coaddition, and (10) final source extraction. For comparison, the online SSC pipeline only performs steps (1), (2), (4), basic filtering, and step (6), and the GeRT includes software for steps (1), (2), (4), and (8). The 10 processing steps are summarized in the following subsections.

3.1. Basic Processing

The optimal processing for step (1) depends on the background, the length of the data ramp (MIPS-Ge data are recorded with nondestructive reads sampled at 0.131 s), and the rate of cosmic rays at the time of the observations. The SSC online pipeline is tuned for the short data ramps (3 s and 4 s). We tuned the pipeline modules (cosmic ray detection and removal and slope estimation) of step (1) to minimize the noise level for the longer 10 s ramps of the S-COSMOS data. The tuning solutions for 70 μm are similar to those derived for the GOODS-North photometry data, which have the same ramp length (Frayer et al.

2006b). MIPS-Ge uses stimulator-flash observations to track the response of each detector as a function of time. After the calculation of the initial stimulator-flash solution, which is basically a linear interpolation between stimulator-flash measurements (step 2), we removed outlier values and rederived a smoothed stimulator-flash solution (step 3). For 70 μm, the stimulator-flash response function was smoothed by about 2 min (slightly longer than the stimulator-flash cycle) to provide the lowest noise. For 160 μm, the solution was smoothed by about 8 min to yield the best results.

In step 4, the BCD data are calibrated as $\mathrm{BCD}(t) = FC[U(t)/\mathrm{SR}(t) - DARK]/IC$, where $U(t)$ is the uncalibrated slope image, $\mathrm{SR}(t)$ is the stimulator-flash response solution derived in step (3), and *DARK* is the dark calibration file. The *IC* calibration file is the illumination correction that corrects for the flat-field response and the nonuniformity of the stimulator flash (Gordon et al. 2005). The flux conversion factor (FC) converts the instrument units into physical surface brightness units of MJy sr^{-1}. For self-consistency, we adopt the same *DARK* and *IC* files used for the official calibration of the MIPS instrument (Engelbracht et al. 2007; Gordon et al. 2007; Stansberry et al. 2007). The calibration *FC* values of 702 MJy sr^{-1} per MIPS-70-unit (Gordon et al. 2007) and 41.7 MJy sr^{-1} per MIPS-160-unit (Stansberry et al. 2007) are adopted. The calibration of MIPS is based on stellar SEDs ($S_\nu \propto \nu^2$). We have placed the data on a constant $\nu\, S_\nu$ scale by dividing the data by the color correction factors of 0.918 and 0.959 for the 70 and 160 μm bands, respectively (Stansberry et al. 2007). These color corrections are appropriate (accurate to better than 2%) for a wide range of galaxy and AGN SEDs ($S_\nu \propto \nu^{-\alpha}$, $\alpha = 0$–3) across the filter bandpass.

3.2. Data Filtering

The optimization of the processing steps (1–4) provided sensitivity improvements of about 20% in comparison with the default parameters, while the filtering (step 5) can provide more than a factor of two improvement in point-source sensitivity. Filtering is key in the removal of systematic instrumental effects that impede the ability to integrate down with deep observations. The two main artifacts impacting MIPS-Ge data are the latents due to the stimulator flashes and variations of the slow response (>2 min) as a function of time. The slow response is removed at 70 and 160 μm by subtracting a running median per detector as a function of time, i.e., a high-pass filter. The latent artifacts due to the stimulator flashes are not fully removed by a simple high-pass filter, since these variations occur on shorter timescales. At 70 μm, the stimulator-flash artifacts are correlated by column. Since the scan direction is nearly along the columns of the array, these artifacts contribute to the streaking within the maps if not corrected. We remove the column residuals by subtracting the median of the values along each column for every BCD at 70 μm. The combination of the column median filter and a high-pass median time filter per detector removes the instrumental artifacts at 70 μm.

There is no equivalent column filter at 160 μm to remove the high-frequency (short time scale) latent images introduced by the stimulator flashes. Fortunately, at 160 μm, these artifacts are repeatable and can be determined by stacking the data as a function of DCENUM (Data-Collection-Event Number) within the stimulator-flash cycle. Since the scan-mirror position also varies with DCENUM within the stimulator-flash cycle, we stacked the data per AOR for each scan-mirror position and took the median value of the stack to derive the correction as a function of detector and scan-mirror position. These corrections were subtracted from the BCDs to remove artifacts due to the stimulator flashes. The combination of this stacking correction and a high-pass median time filter removes the instrumental artifacts at 160 μm.

With the S-COSMOS data, we tuned the filtering techniques (step 5) to minimize the noise in the output maps. For both 70 and 160 μm, the short time scale stimulator-flash artifacts were removed first, followed by a high-pass median time filter to remove the longer time scale transients. We adopted a time filter width of 12 frames (2 min) to yield the best results. After the initial filtering, the brightest sources have negative "side-lobes" in the maps since bright sources bias the calculation of the median for neighboring pixels. To remove these filtering artifacts, the filtering was done in two passes. The data from the first filtering pass (step 5) were coadded (step 6), and sources were extracted (step 7) to find the location of the bright sources. The source positions within the original BCDs were masked and new filtering corrections were calculated in a second pass, ignoring the pixels containing sources. This two-pass filtering technique minimizes the artifacts while preserving the point-source calibration. After the second filtering pass (step 8), the data were coadded to produce the final maps (step 9, Section 3.3) and sources were extracted to produce the catalogs (step 10, Section 3.4).

3.3. Imaging

The SSC mosaicking software (MOPEX, version 16.3.7; Makovoz & Marleau 2005) was used to combine the data and make the final images. A fast plane-to-plane coordinate transformation method was used to project the data onto the sky (Makovoz 2004) with the default MOPEX interpolation scheme. We carried out the imaging steps following the techniques discussed for the xFLS MIPS-Ge data (Frayer et al. 2006a). An important improvement available after the processing of the xFLS data is a more robust outlier rejection technique within MOPEX. The updated method rejects data around the median of a data stack for each sky pixel instead of rejecting data with respect to the average of the data stack. This enables more aggressive outlier rejection without compromising the calibration of point sources. The best sensitivity was obtained using rejection thresholds of $\pm 2.5\sigma$. The new outlier rejection method improved the sensitivity in the maps by about 5%.

The pipeline uncertainties of the BCDs and integration times were not used as weights in the coaddition of the data; all of the data (155,411 BCDs in total) flagged as good were given equal weight. Bad data flagged on a detector basis during the pipeline processing or identified as outliers by MOPEX were not included. The vast majority of the data were taken with 10 s integrations and no correction is needed for the 4 s BCDs (all BCDs are calibrated correctly in MJy s^{-1}). The pipeline uncertainties (calculated from the formal error propagation of the pipeline steps) do not fully represent the actual noise characteristics of the data, and underestimate the real noise slightly in low background regions. The main utility of the pipeline uncertainties for these data is to provide a lower limit to the input noise for the MOPEX outlier rejection algorithm.

3.4. Source Detection and Extraction

Sources were detected and extracted from the final images using the Astronomical Point-Source Extraction (APEX) tools within the MOPEX software package and using additional

specialized scripts. For optimal source detection and extraction, accurate background subtraction and noise estimates are needed. The filtering process (steps 5 and 8) yields a small systematic negative offset of the background level in the image. This offset was estimated by taking the median of the image within the central regions after masking sources detected at levels greater than 3σ. After the removal of the global offset level (-0.05 MJy sr^{-1} at 70 μm and -0.07 MJy sr^{-1} at 160 μm), there are still local background fluctuations across the image depending on the local density of sources (both from detected sources and undetected/confused sources associated with infrared galaxies seen at 24 μm). The local background level was derived by taking a median within a box around each pixel (after masking sources detected at levels greater than 3σ). For source detection, we used a small box with a linear size of 5 Full-Width Half-Maximum (FWHM) widths to remove the local background, and for source extraction (fitting) we used a larger background box with a size of 9–10 FWHM widths to conserve the calibration.

Several types of noise images can be produced by the MOPEX and APEX software, but none are optimal for these data. The "std" noise image produced by MOPEX represents the empirical scatter from the repeated observations per sky pixel divided by the square root of the number of good observations. For deep observations, the "std" file underestimates the true noise since it does not account for the pixel-to-pixel correlated noise or the confusion noise. APEX computes the spatial pixel-to-pixel noise ("noise" file) by calculating the noise within a local box surrounding each pixel after rejecting positive outliers. The output "noise" image has variations that depend on the outlier parameter and the number of sources within the local box. To avoid local biases due to sources, we derived a "noise" image after the extraction of sources, adopting a box size with a linear scale of 9–10 FWHM widths (the same size used for the local background subtraction for source fitting). To preserve both the small- and large-scale spatial variations of the uncertainty across the science image, both the "std" (representing small-scale variations) and "noise" (representing large-scale variations) files were used. The quality of "std" and "noise" images was first improved by smoothing the images by 1 and 3 FWHM widths, respectively, and then combined in quadrature. Equal weights were given to the "std" and "noise" images at 70 μm. Since the confusion noise is important at 160 μm, the weights at 160 μm were based on the relative contributions of the instrument and the confusion noise (Section 5.2). The std image was given a weight corresponding to the instrument noise, and the noise image was given a weight corresponding to the confusion noise to produce the combined uncertainty file at 160 μm. The median level of the combined uncertainty file was scaled to match the total average noise level derived from fitting the 1σ width of a Gaussian to the data histogram of the image after source extraction. Source extraction and noise estimates were repeated until the results converged.

After proper background subtraction and deriving an accurate uncertainty image, sources were detected using the APEX peak algorithm. Peaks with a signal-to-noise ratio (S/N) of greater than 3 were fitted using the Point-source Response Function (PRF, which includes the effects of the detector size and the adopted subsampling of the detectors) image. At the spatial resolution of the MIPS-Ge bands, the PRF is stable. At 70 μm, we adopt the PRF (FWHM = 18″.6) made previously from the xFLS data (Frayer et al. 2006a). At 160 μm, we made a new PRF using the COSMOS, xFLS, and the data from all of the fields from the *Spitzer* Wide-area Infrared Extragalactic Legacy

Survey (SWIRE; Lonsdale et al. 2004). None of the individual fields has a large number of isolated 160 μm sources with a high S/N to make a high-quality PRF. At 160 μm, the brightest sources ($\gtrsim$ 2 Jy) cannot be used due to the nonlinearity of the detectors (Stansberry et al. 2007). In total, we used 149 isolated sources from the *Spitzer* 160 μm surveys, which have S/N $\gtrsim$ 30 and $S160 < 1$ Jy[9] to produce an empirical PRF (FWHM = 39″).

The detection and extraction of sources was done in multiple passes. Initial source lists were visually analyzed and cleaned to remove sources with low coverage and potential spurious sources in the Airy rings around bright sources. The detection table was updated to remove bad sources, and source fitting was redone. In the few cases where the detection routine failed in the proper deblending of two or more sources, the detection table was modified and source-fitting measurements were redone using better initial source positions.

3.5. Astrometry

The absolute pointing reconstruction of the *Spitzer* telescope is typically better than 1″. The pointing uncertainties are much less than the large FWHM width of the data (18″.6 at 70 μm and 39″ at 160 μm). We verified the pointing solutions by comparing the positions of the 70 μm sources with their VLA radio counterparts (Schinnerer et al. 2007). For the approximately 400 sources detected at S/N > 5 at both 1.4 GHz and 70 μm, we find an average positional difference (*Spitzer*—VLA) of ΔR.A. $= -0.08 \pm 0″.08$ and ΔDecl. $= 0.17 \pm 0″.08$. These small offsets are well within the scatter measured for individual sources of 1–2″, so no positional corrections were made to the data.

3.6. Calibration

MIPS is calibrated assuming the point-spread function (PSF, which does not include the effect of the detector size) calculated using the *Spitzer* TinyTim (S-TinyTim) models (Krist 2002). The modeled PSFs have been shown to match the observations for all bands (Engelbracht et al. 2007; Gordon et al. 2007; Stansberry et al. 2007). An important aspect of the MIPS PSFs is that significant flux arises outside of the first Airy ring on large spatial scales. We corrected the derived flux densities for emission outside of the adopted PRF images using the S-TinyTim models. For the adopted PRFs (87″ × 87″ at 70 μm and 190″ × 190″ at 160 μm), we derive an aperture correction of 1.15 at both wavelengths based on modeled PSFs assuming a constant νS_ν SED. Empirically, it is difficult to measure the level of emission outside of the first Airy ring for MIPS-Ge data. However, the calibration factors assume the modeled PSFs out to very large spatial scales, and we must apply this correction for consistency. We verified the calibration consistency of our techniques using archived calibration observations taken over the lifetime of the mission. For comparison, observations of the calibration star HD180711 ($S70 = 447.4$ mJy; Gordon et al. 2007) were used at 70 μm, while observations of the ULIRG IRAS 03538–6432 were used at 160 μm (Stansberry et al. 2007; Klaas et al. 2001, $S160 = 1.04$ Jy). Using an aperture correction for a modeled PSF with a stellar SED and similar reduction techniques carried out for S-COSMOS, we measure a flux density of 450 ± 18 mJy for HD180711. This is consistent with expectations (flux density ratio of 1.01 ± 0.04). At 160 μm, we measure a flux density ratio of 0.97 ± 0.05 compared

---

[9] Throughout this paper, the flux densities of the MIPS bands are defined as $S160 = S_\nu(155.9\ \mu m)$, $S70 = S_\nu(71.4\ \mu m)$, and $S24 = S_\nu(23.7\ \mu m)$.
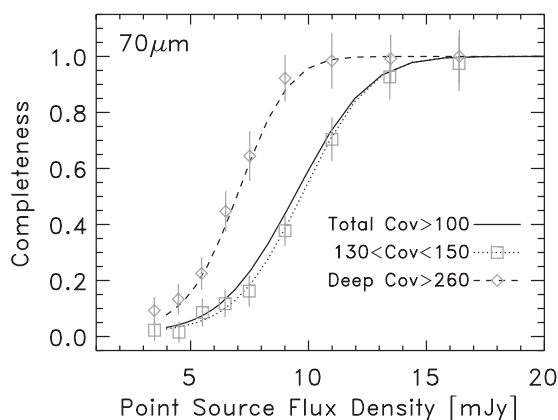
Figure 3. The 70 μm completeness levels (S/N $\geqslant$ 5.0) as a function of flux density and coverage. The effective average completeness level used for the source counts is given by the solid line (Total Cov > 100). Simulation results for the deep area (Cov > 260) and typical coverage values (130 < Cov < 150) are shown by the gray diamonds and squares. The dashed and dotted lines represent the expected completeness level based on the S/N threshold for the regions used in the simulations.

Figure 4. The 160 μm completeness levels (S/N $\geqslant$ 5.0) as a function of flux density and coverage. The effective average completeness level used for the source counts is given by the solid line (Total Cov > 20). Simulation results for the deep area (Cov > 50) and typical coverage values (25 < Cov < 33) are shown by the gray diamonds and squares, along with the expected completeness level based on the S/N threshold and coverage values (dashed and dotted lines respectively)

to expectations for IRAS 03538-6432 using similar reduction techniques carried out for S-COSMOS. These results suggest that the calibration of the S-COSMOS data is consistent with the MIPS calibration papers; the absolute calibration uncertainty of MIPS is 5% at 70 μm (Gordon et al. 2007) and 12% at 160 μm (Stansberry et al. 2007).

3.7. Corrections for Completeness and Eddington Bias

The completeness levels were estimated by simulations and calculations based on the S/N threshold. For the simulations, sources were injected at random locations into the images and extracted using the same techniques adopted for the production of the catalogs. For high S/N $\geqslant$ 5.0, the S/N threshold itself is the dominant effect in the determination of the completeness level. At lower S/N, other effects such as the details associated with source detection and fitting become significant. The completeness levels vary significantly across the image as a function of coverage and flux density. Based on the S/N $\geqslant$ 5.0 threshold, the average effective completeness level across the image can be calculated as a function of flux density as the fractional area within the image for which $S + I \geqslant 5.0U$, where S is the flux density, I is the science image, and U is the uncertainty image. Figures 3 and 4 show completeness calculations as a function of flux density and coverage. The simulations match the expected curves very well at 70 μm for both the deep and typical regions within the image. For the deep region at 160 μm, the simulated completeness values are relatively noisy and are lower than expected for 60–90 mJy, potentially due to the effects of confusion and/or the small number of independent beams within the simulated area. The completeness calculations at 160 μm for the nominal coverage of greater than 20 are similar to the simulations and the calculations for the typical range of coverage values (25–33). For the derivation of the S-COSMOS source counts (Section 5.1), we adopt the completeness curves for coverages greater than the nominal values of 100 and 20 at 70 and 160 μm, respectively (solid lines, Figures 3 and 4).

In addition to the completeness corrections, the counts are affected by the Eddington bias (flux boosting). At faint flux densities, the observed flux densities are slightly higher on average than the true flux densities since sources on positive noise features are preferentially selected. This effect of "flux

boosting" is not as important for S/N $\geqslant$ 5 as for lower S/N, but would still yield a small systematic bias in the measured counts if not corrected. The same simulations used to help quantify the completeness corrections were used to check the importance of the Eddington bias. The ratio of the observed to input flux densities ($S_{\rm obs}/S_{\rm true}$) of each bin was measured for both the deep region and the wide area with "full-blown" simulations that injected sources at random positions within the image (one at a time) and exacted the output flux densities using the same methods adopted to produce the source catalogs. Given the variation of coverage in the data, it is difficult to obtain sufficient statistics as a function of flux density and coverage across the image using these full-blown simulations (as was the case for the completeness estimates). Instead, we carried out simpler calculations that were consistent with the full-blown simulations, but are significantly more accurate. Input flux densities ($S_{\rm true}$) with the same power-law distribution as the observed source counts were randomly added to the noise distribution given by the uncertainty image, and the output observed flux densities were derived. The effective Eddington bias of $S_{\rm obs}/S_{\rm true}$ was calculated over the entire image for each flux density bin for the adopted S/N $\geqslant$ 5 cut and used to correct the observed flux densities for the derivation of the counts (Section 5.1). This method fully accounts for the variation of coverage and noise across the image.

4. PRODUCTS

The S-COSMOS 70 and 160 μm products are available online at the NASA Infrared Science Archive (IRSA) at the Infrared Processing and Analysis Center (IPAC). The products described here are version 3 of the data. Version 1 and version 2 were early quick-look products based on simplified reductions of subsets of the observations. Version 3 represents the combination of all data from the S-COSMOS MIPS program and is the first version to be calibrated properly and processed with the best-known data reduction techniques.

4.1. Images

The science images have been background subtracted with the removal of a global offset, but the local background fluctuations have not been removed (Section 3.4). The images are in surface-brightness units of MJy sr^{-1} assuming the latest calibration and

Table 2
Summary of Product Properties

Property	70 μm	160 μm
Image pixel scale	4″	8″
Image FWHM resolution	18″.6	39″
Nominal coverage level	100	20
Median coverage[a]	140.3	28.3
Median exposure time[a]	1350 s	273 s
Surface-brightness noise (1σ)[a]	0.13 MJy sr^{-1}	0.18 MJy sr^{-1}
Point-source noise (1σ)[a]	1.7 mJy	13 mJy
Area mapped[a]	2.471 deg^2	2.438 deg^2
Number of sources ($\geqslant 5.0\sigma$)	1512	499

Notes.
[a] Measured properties for coverages (number of observations) larger than the nominal coverage level.

have been color corrected to match SEDs with a constant νS_ν scale (Section 3.1). The uncertainty images have also been color corrected and are in units of MJy sr^{-1}. The uncertainty images (1σ) represent both the small-scale and large-scale spatial noise properties associated with the science image (Section 3.4).

The coverage maps provide the effective number of observations (after data editing) per point on the sky for the science images. At 70 μm for the nominal coverage of greater than 100, the median effective exposure time is 1350 s, while the ultradeep region with a coverage of greater than 250 has an exposure time of 2800 s. At 160 μm for the nominal coverage of greater than 20, the median effective exposure time is 273 s, while the ultra-deep region with a coverage of greater than 50 has an effective exposure time of 567 s.

Table 2 lists the image properties and sensitivities. The sensitivities represent the total noise, including confusion. The surface-brightness noise for the adopted pixel scale was derived from fitting the 1σ width of a Gaussian to the data histogram of the image after source extraction. To derive the effective point-source noise, including the effects of correlated noise between the pixels, we carried out aperture measurements at random locations within the residual image after the extraction of sources. We derive conversion factors between the point-source noise and surface-brightness noise of 13.3 ± 1.3 mJy (MJy sr$^{-1})^{-1}$ and 74 ± 7 mJy (MJy sr$^{-1})^{-1}$ for the 70 μm and 160 μm images, respectively. The average point-source noise (1σ) is 1.7 mJy and 13 mJy at 70 and 160 μm, respectively. These point-source values include the aperture correction of 1.15 for emission outside of the measured PRF (Section 3.6).

4.2. Catalogs

Point-source catalogs were made for a S/N $\geqslant$ 5.0. In total, 1512 sources at 70 μm (Table 3) and 499 sources at 160 μm (Table 4) are cataloged. The catalogs are single-band source lists and are independent from each other and the MIPS 24 μm data. Although the catalogs are not biased by data at other wavelengths, we did use the 24 μm and radio data to confirm the reliability of the catalogs. Within the central area cataloged at 24 μm, only seven 70 μm sources do not have a 24 μm counterpart ($S24 > 60\,\mu$Jy) within the approximate 70 μm beam radius of 9″ (which corresponds to a relatively large chance positional coincident of about 50% for a 24 μm source). Of these seven, four are associated with a radio source, two do not have a radio counterpart, and one is outside the radio coverage. For the three cases without a current 24 μm or radio counterpart, the 70 μm position is located between a blend of two or three 24 μm sources. These blended sources could represent valid

detections at 70 μm. All 160 μm sources have possible 24 μm counterparts, which is not unexpected given the low spatial resolution of the 160 μm data (where on average there are about three 24 μm sources per 160 μm beam). Although we find no obvious spurious detections within the catalogs, users should be cautious and check the images when comparing catalogs at different wavelengths due to potential source blending. Tables 3 and 4 show the format for an example portion of the S-COSMOS 70 μm and 160 μm catalogs published in the online version of the journal.

PRF-fitting flux densities and aperture measurements were made using the APEX software. The aperture and PRF measurements are in statistical agreement. Since PRF measurements are significantly more accurate for faint sources (e.g., Frayer et al. 2006a), the PRF flux densities are used for the vast majority of sources (flag of "p"). Aperture measurements are adopted for sources not reasonably well fitted by the PRF (extended sources or unresolved blends) and are given a flag of "a" within the catalog. Resolved blends fitted well by multiple PRFs are given a flag of "p." For the one blend of two resolved sources that is not fitted well by two point sources at 70 μm, the total aperture flux is divided among the two components based on their relative peaks (flag of "ap"). For consistency with the adopted calibration of MIPS, the measurements include the aperture correction of 1.15 for emission outside of the measured PRF (Section 3.6). No corrections for flux nonlinearity have been made (Stansberry et al. 2007). Only one source (SCOSMOS160 J100027.0+032226, $S160 \sim 11$ Jy) is bright enough to be significantly impacted by flux nonlinearity (the only source at 160 μm with an aperture measurement, flag of "a"); its flux density should be treated with caution.

The errors on the fitted flux densities derived by APEX are not used since they are underestimated by about a factor of three for these data. We adopt errors based on the S/N measurements that represent the fitted peak flux density divided by the uncertainty image at the location of the source. The errors on the measured flux densities (S) represent the random errors given by the S/N combined with the systematic calibration uncertainty (ϵ_{cal}). The flux density error $\sigma(S) = (1/[S/N] + \epsilon_{cal})S$, where ϵ_{cal} is 0.05 and 0.12 for the MIPS 70 μm (Gordon et al. 2007) and MIPS 160 μm (Stansberry et al. 2007) bands, respectively. The few sources (nine) requiring large aperture measurements have additional measurement errors of 10%–20%.

We find that the positional fitting errors calculated by APEX are 2.0 times larger on average than the expected radial positional errors of ≈ 0.6 (FWHM/[S/N]) given by Condon (1997) for all S/Ns. We adopt the APEX errors, but treat them as 2σ uncertainties. For these data, the relationship of Condon (1997) is appropriate for typical S/Ns, but underestimates the errors for the highest S/Ns. We adopt a floor on the uncertainty of $\epsilon_{pos} = 0.5$ pixel ($\simeq 0.1$ FWHM; Table 2), representing the difficulty in deriving positions to better than a fractional pixel regardless of the S/N. The cataloged radial positional errors (2σ uncertainties) are given by $(\sigma_x^2 + \sigma_y^2 + \epsilon_{pos}^2)^{0.5}$, where σ_x and σ_y are the fitting errors in the x–y plane derived by APEX.

5. RESULTS AND DISCUSSION

5.1. Source Counts

The source counts were derived from S/N $\geqslant$ 5.0 source lists corrected for completeness over the region within the images with high coverage (> 100 at 70 μm and > 20 at 160 μm), corresponding to an effective survey area for the 70 and 160 μm

Table 3
Spitzer COSMOS 70 μm Catalog

Source Name	α (J2000) (deg)	δ (J2000) (deg)	Error (arcsec)	S70 (mJy)	$\sigma(S70)$ (mJy)	S/N	Flag
(1)	(2)	(3)	(4)	(5)	(6)	(7)	(8)
SCOSMOS70 J095546.9+013605	148.945497	1.601560	5.0	20.6	4.9	5.3	p
SCOSMOS70 J095552.5+014243	148.968967	1.712061	2.2	226.2	21.9	21.3	p
SCOSMOS70 J095605.9+014443	149.024976	1.745507	4.7	17.1	3.9	5.7	p
SCOSMOS70 J095610.1+014213	149.042376	1.703652	4.8	14.3	3.4	5.4	p
SCOSMOS70 J095615.0+014315	149.062575	1.720973	4.0	16.6	3.2	7.1	p

Notes. Column 1 gives the source names following the IAU designations. Columns 2 and 3 are the right ascension (α) and declination (δ) J2000.0 source positions in decimal degrees. Column 4 is the radial positional uncertainty in arcsec (2σ). Column 5 is the total flux density measurement in mJy. Column 6 is the flux density error in mJy (1σ), including the systematic uncertainty of the absolute flux density scale. Column 7 is the S/N of the peak. Column 8 is the flag for the flux density measurement method. A flag of "p" indicates that the source was fitted by the PRF, "a" indicates an aperture measurement with a diameter of 96″, and "ap" indicates an aperture measurement whose flux was divided between two components based on the relative strengths of their peaks.

(This table is available in its entirety in machine-readable and Virtual Observatory (VO) forms in the online journal. A portion is shown here for guidance regarding its form and content.)

Table 4
Spitzer COSMOS 160 μm Catalog

Source Name	α (J2000) (deg)	δ (J2000) (deg)	Error (arcsec)	S160 (mJy)	$\sigma(S160)$ (mJy)	S/N	Flag
(1)	(2)	(3)	(4)	(5)	(6)	(7)	(8)
SCOSMOS160 J095619.9+012425	149.083255	1.407074	9.2	134.9	40.1	5.6	p
SCOSMOS160 J095621.2+015951	149.088411	1.997640	9.7	122.5	37.2	5.4	p
SCOSMOS160 J095635.5+014332	149.147947	1.725679	9.2	122.7	35.4	5.9	p
SCOSMOS160 J095635.7+012544	149.149042	1.429048	4.7	1073.7	188.5	18.0	p
SCOSMOS160 J095636.9+015415	149.153962	1.903362	5.0	1093.4	209.8	13.9	p

Notes. Column headers are the same as described in Table 3 for Columns 1–7. Column 8 is the flag for the flux density measurement method, where "p" indicates a PRF measurement and "a" indicates an aperture measurement with a diameter of 4′.

(This table is available in its entirety in machine-readable and Virtual Observatory (VO) forms in the online journal. A portion is shown here for guidance regarding its form and content.)

fields of 2.471 and 2.438 deg^2, respectively. The public catalogs presented in Section 4.2 include sources outside of this nominal area with a lower coverage. The effective completeness value for each flux density bin was computed by integrating over the completeness curves (Figures 3 and 4) as a function of flux density across each bin with weights based on the measured slope of the source counts.

Figures 5 and 6 show the Euclidean-normalized differential source counts ($dN/dS \times S^{2.5}$) at 70 μm and 160 μm, and the results are tabulated in Tables 5 and 6, respectively. The counts are calculated for independent flux density bins. The error bars represent the Poisson errors associated with the number of sources and the uncertainties on the completeness corrections. The gray region shows the range of values implied from the most statistically accurate counts within each flux density bin, including the additional uncertainty due to the systematics associated with the calibration of MIPS (5% at 70 μm and 12% at 160 μm).

At 70 μm, the S-COSMOS counts are measured down to a level of 10 mJy, which is near the peak of the Euclidean-normalized differential source counts (Frayer et al. 2006b). The faint ($\sim$ 10 mJy) S-COSMOS counts at 70 μm (Figure 5) agree with those measured for GOODS-N (Frayer et al. 2006b) and the xFLS (Frayer et al. 2006a). The bright counts for S-COSMOS also agree with the measurements from the SWIRE survey. At intermediate flux densities of around 20–30 mJy, the counts for S-COSMOS are slightly lower than those found for the xFLS and model predictions of Lagache et al. (2004). All the counts
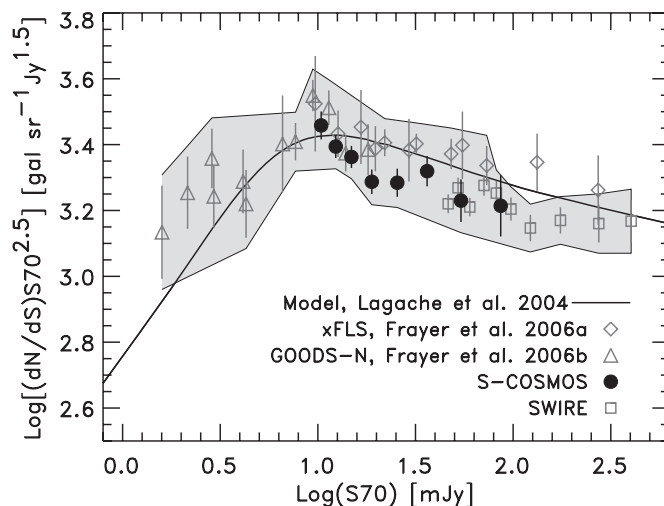
Figure 5. Euclidean-normalized differential source counts at 70 μm compared with the evolutionary model of Lagache et al. (2004) (solid line). The S-COSMOS and SWIRE counts are new measurements. The xFLS and GOODS-N counts are from Frayer et al. (2006a, 2006b) respectively. All data are on the same calibration scale. The gray region shows the range of values for the accurate data points within each flux bin and includes the additional systematic uncertainty associated with the calibration at 70 μm (5%).

have been placed on the same scale by matching the calibration, color corrections, and the PRF adopted for S-COSMOS. The correction factors for the other data sets are given in Table 7.

Table 5
S-COSMOS 70 μm Source Counts

Observed Average S_ν	S_{low}	S_{high}	Observed Number	Completeness	Eddington Bias	$dN/dS\ S^{2.5}$
(mJy)	(mJy)	(mJy)				(gal sr^{-1} Jy$^{1.5}$)
11.02	10	12	245	0.68 ± 0.05	1.06	2872 ± 280
12.84	12	14	186	0.90 ± 0.03	1.04	2478 ± 199
15.30	14	17	180	0.98 ± 0.02	1.03	2304 ± 178
19.08	17	22	144	1.00 ± 0.02	1.01	1937 ± 166
25.76	22	30	108	1.00 ± 0.02	1.01	1924 ± 189
36.26	30	45	92	1.00 ± 0.02	1.00	2086 ± 221
54.05	45	70	46	1.00 ± 0.02	1.00	1697 ± 252
86.36	70	110	22	1.00 ± 0.02	1.00	1637 ± 350

Notes. The counts are based on the $\geqslant 5.0\sigma$ catalog and were measured for an area of 2.471 deg^2 with a coverage of greater than 100 observations. The counts were corrected for completeness and the Eddington bias ($S_{\text{obs}}/S_{\text{true}}$). The tabulated uncertainties for the differential counts ($dN/dS\ S^{2.5}$) include the Poisson noise and the completeness uncertainties, but do not include the additional systematic uncertainty (5%) associated with the calibration of the MIPS 70 μm band.

Table 6
S-COSMOS 160 μm Source Counts

Observed Average S_ν	S_{low}	S_{high}	Observed Number	Completeness	Eddington Bias	$dN/dS\ S^{2.5}$
(mJy)	(mJy)	(mJy)				(gal sr^{-1} Jy$^{1.5}$)
65.05	60	70	82	0.63 ± 0.05	1.09	16619 ± 2260
74.82	70	80	83	0.85 ± 0.03	1.08	17875 ± 2060
89.01	80	100	83	0.95 ± 0.02	1.06	12713 ± 1420
139.18	120	160	40	1.00 ± 0.02	1.02	9445 ± 1505
187.72	160	250	29	1.00 ± 0.02	1.01	6526 ± 1218

Notes. The counts are based on the $\geqslant 5.0\sigma$ catalog and were measured for an area of 2.438 deg^2 with a coverage of greater than 20 observations. The counts were corrected for completeness and the Eddington bias ($S_{\text{obs}}/S_{\text{true}}$). The uncertainties for the differential counts ($dN/dS\ S^{2.5}$) include the Poisson noise and the completeness uncertainties, but do not include the additional systematic uncertainty (12%) associated with the calibration of the MIPS 160 μm band.
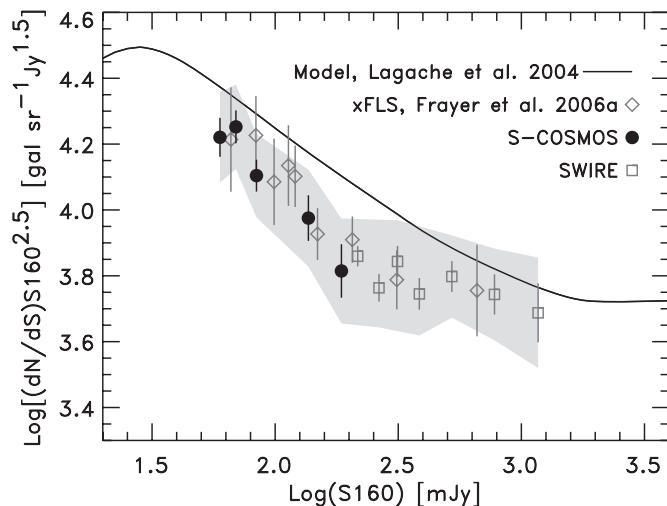
Figure 6. Euclidean-normalized differential source counts at 160 μm compared with the evolutionary model of Lagache et al. (2004) (solid line). The S-COSMOS and SWIRE counts are new measurements, while the xFLS counts are from Frayer et al. (2006a). All data are on the same calibration scale. The gray region shows the range of values for the accurate data points within each flux bin and includes the additional systematic uncertainty associated with the calibration at 160 μm (12%).

The previous results for the xFLS, SWIRE, and GOODS-N did not include the aperture correction for the flux density outside

of the measured PRF. The counts for SWIRE are based on the public catalogs (2005 November, Data Release 3 [DR3]), which cover 49 deg^2. The SWIRE counts at 70 or 160 μm have not previously been published and are presented here to constrain the counts at the brightest flux densities. Only the high S/N ($\gtrsim 10$) SWIRE sources with completeness levels near one are presented in Figures 5 and 6.

At 160 μm, the S-COSMOS counts are measured down to a level of 60 mJy. Measurements of deeper counts are limited by confusion (Section 5.2). The measured counts at 160 μm agree with the counts measured previously in the xFLS (Frayer et al. 2006a) and the counts derived here based on the SWIRE survey. As done for 70 μm, all counts are placed on the current calibration scale (Table 7). These correction factors also include a decrease in the flux densities due to the new PRF derived here (Section 3.4). The previous PRF images used by the xFLS and SWIRE surveys are affected by the flux nonlinearity for bright sources at 160 μm.

The faintest ($S160 < 80$ mJy) and brightest ($S160 > 500$ mJy) source counts are consistent with the Lagache et al. (2004) model, but the observed counts for all three surveys at intermediate flux densities are about a factor of 1.5 times lower than the model implies. The observed 160 μm counts show a steep increase in the differential counts for decreasing flux densities ($dN/dS \propto S^{-3.5\pm0.2}$) for $S160 < 150$ mJy. The slope for the faint (10–20 mJy) S-COSMOS 70 μm source counts ($dN/dS \propto S^{-3.1\pm0.2}$) is roughly consistent with the

Table 7
Scaling Factors for MIPS-Ge Surveys

Survey, Version	70 μm	160 μm
S-COSMOS, versions 1 and 2	1.25	1.07
S-COSMOS, version 3	1.00	1.00
xFLS(Frayer et al. 2006a)	1.20	0.97
SWIRE (2005 November, DR3)	1.10	0.98
GOODS-N(Frayer et al. 2006b)	1.15	$\cdots$

Notes. Multiplicative scaling factors required to place catalogs on the same calibration scale derived for the official calibration of MIPS (Gordon et al. 2007; Stansberry et al. 2007) and used here for the S-COSMOS, version 3 products. Factors include the combination of color corrections, calibration updates, PRF updates, and the aperture correction for emission outside of the measured PRF.

160 μm slope and is slightly steeper than the model predictions. The differences between the model and the source counts at 70 μm are not as clear as those seen at 160 μm. The results for 160 μm may suggest the importance of galaxies having more cold dust than assumed in the models. Observations with the future *Herschel* telescope should provide better constraints on the FIR SEDs of distant galaxies.

5.2. Confusion Level of the MIPS 70 and 160 μm Bands

The S-COSMOS 70 μm data are dominated by instrument uncertainties and are not deep enough to constrain the confusion noise. Frayer et al. (2006b) measured the MIPS 70 μm confusion noise based on the much deeper 70 μm observations of GOODS-North. Based on Frayer et al. (2006b) and the calibration scaling factors (Table 7), the updated extragalactic confusion noise level for the MIPS 70 μm band is $\sigma_c = 0.35 \pm 0.15$ mJy ($q = 5$), including the updated systematic error on the flux calibration.

In contrast to the 70 μm data, the S-COSMOS 160 μm data contain a significant noise component due to confusion. We estimate the confusion noise at 160 μm following the empirical technique performed at 70 μm (Frayer et al. 2006b). A direct empirical measurement of the confusion noise for the MIPS 160 μm band has not been published previously. Dole et al. (2004) report a confusion level at 160 μm based on the techniques of Dole et al. (2003) and the models of Lagache et al. (2004). They find that the predicted confusion noise from their models is in reasonable agreement with the observations, assuming that the instrumental noise (σ_I) follows the theoretical MIPS model and integrates down as $\sigma_I \propto t^{-0.5}$. However, the early processing of MIPS-Ge data was not optimal, and an accurate empirical measurement of the total instrumental noise (including photon noise, detector noise, and noise associated with the data processing) is required to measure the confusion level.

The instrument noise was estimated empirically by subtracting pairs of data subsets with the same integration time and covering the exact same region on the sky (which removes sources and any remaining cirrus structure after filtering). We fit the instrument noise measurements as a function of integration time for combinations of deep pairs of data sets and obtain $\sigma_I \propto t^{-0.49 \pm 0.03}$. This result is consistent with idealized data ($\sigma \propto t^{-0.5}$) and highlights the success of the reduction methods in removing systematic artifacts. The extrapolation of instrument noise for half of the data to the full data set yields $\sigma_I = 0.1134 \pm 0.0033$ MJy sr^{-1}, where the uncertainty represents the rms measurement error combined in quadrature with the error associated with the extrapolation.

Following the terminology of Dole et al. (2003), the total noise (σ_T) represents the noise after the extraction of sources above a limiting flux density (S_{lim}), and the photometric confusion noise (σ_c) represents fluctuations due to sources with flux densities below S_{lim}. The confusion noise is given by $\sigma_c = (\sigma_T^2 - \sigma_I^2)^{0.5}$, which is appropriate for an approximate Gaussian distribution of the noise after the extraction of sources. We iterate between source extraction at different limiting flux densities and confusion noise measurements until we converge to a solution with $q \equiv S_{\mathrm{lim}}/\sigma_c = 5$. For the $q = 5$ solution, we derive $\sigma_T = 0.1772 \pm 0.0089$ MJy sr^{-1} and $\sigma_c = 0.1362 \pm 0.0119$ MJy sr^{-1}, for a limiting source flux density of $S160 = 50$ mJy.

Noise measurements in surface brightness units (MJyr sr^{-1}) depend on the pixel scale, and all measurements here are based on the 8$''$ pixel scale of the 160 μm image. The uncertainties on the noise measurements given in MJy sr^{-1} also do not include the 12% systematic calibration uncertainty. Including the systematic calibration uncertainty and the measured conversion between surface-brightness noise and point-source noise (Section 4.1), the point-source confusion level of the MIPS 160 μm band within the COSMOS field is $\sigma_c = 10.0 \pm 3.1$ mJy. The systematic uncertainties contribute 71% to the total error budget, while the random errors contribute 29% to the total error budget.

The measured confusion noise is not entirely due to galaxies. Unlike the case for the MIPS 70 band μm (e.g., Dole et al. 2003; Frayer et al. 2006b), Galactic cirrus is not negligible at 160 μm. We estimate the level of confusion due to Galactic cirrus for the MIPS 160 μm band using the background estimates from the *Spitzer* tool for planning observations (SPOT), which is based on the interstellar medium (ISM) maps from the Diffuse Infrared Background Experiment (Schlegel et al. 1998). At the effective wavelength of 155.9 μm of the MIPS 160 μm band, the ISM background in the direction of the COSMOS field is about 2 MJy sr^{-1}. Using the calculations of Jeong et al. (2005), this background level corresponds to an ISM confusion noise of $\sigma_c(\mathrm{ISM}) \simeq 3.4$ mJy. Hence, the confusion noise due to unresolved galaxies is $\sigma_c(\mathrm{gal}) = (\sigma_c^2(\mathrm{total}) - \sigma_c^2(\mathrm{ISM}))^{0.5} = 9.4 \pm 3.3$ mJy.

The derived confusion limit agrees fairly well with predictions. Dole et al. (2004) report a Source Density Criterion (SDC) limit of 40 mJy ($\sigma_c(q_{\mathrm{SDC}} = 3.8) = 10.6$ mJy) based on the model predictions of Lagache et al. (2004). For a direct comparison with the empirical measurement, the Dole & Lagache et al.'s predictions suggest $\sigma_c(q = 5) = 12.5$ mJy. We find an extragalactic confusion level for the MIPS 160 μm band of $\sigma_c(q = 5) = 9.4 \pm 3.3$ mJy, which is just slightly lower than the predicted value.

6. CONCLUDING REMARKS

We present the 70 and 160 μm observations of the COSMOS field and describe the products. This is the first extragalactic survey available to the public at 70 and 160 μm that has been placed on the calibration scale derived from the recent MIPS calibration papers. We provide updated correction factors for the previously released catalogs of the xFLS (Frayer et al. 2006a) and SWIRE (Lonsdale et al. 2004) programs. Counts are presented based on the S-COSMOS and previous surveys and are found to be in reasonable agreement with the model of Lagache et al. (2004). However, the faint 160 μm source counts are significantly steeper than model predictions. We measure an empirical extragalactic confusion noise level of $\sigma_c = 9.4 \pm 3.3$ mJy ($q = 5$) for the MIPS 160 μm band. In comparison, the

expected confusion noise at 160 μm for *Herschel* is about 1.5–2 mJy (*Herschel* Observation Planning Tool, HSPOT, version 3.4). Future observations with the *Herschel* telescope should constrain the counts and far-infrared properties better than can be done currently due to confusion for the MIPS 160 μm band.

REFERENCES

Capak, P., et al. 2007, ApJS, 172, 99
Condon, J. J. 1997, PASP, 109, 166
Dale, D. A., et al. 2005, ApJ, 633, 857
Dole, H., Lagache, G., & Puget, J.-L. 2003, ApJ, 585, 617
Dole, H., et al. 2004, ApJS, 154, 93
Engelbracht, C. W., et al. 2007, PASP, 119, 994
Frayer, D. T., et al. 2006a, AJ, 131, 250
Frayer, D. T., et al. 2006b, ApJ, 647, L9
Gordon, K. D., et al. 2005, PASP, 117, 503
Gordon, K. D., et al. 2007, PASP, 119, 1019
Hasinger, G., et al. 2007, ApJS, 172, 29
Jeong, W.-S., Mok Lee, H., Pak, S., Nakagawa, T., Minn Kwon, S., Pearson, C. P., & White, G. J. 2005, MNRAS, 357, 535
Klaas, U., et al. 2001, A&A, 379, 823
Koekemoer, A. M., et al. 2007, ApJS, 172, 196
Krist, J. 2002, Tiny Tim/*SIRTF* User's Guide (Pasadena, CA: SSC)
Lagache, G., et al. 2004, ApJS, 154, 112
Lonsdale, C., et al. 2004, ApJS, 154, 54
Makovoz, D. 2004, PASP, 116, 971
Makovoz, D., & Marleau, F. R. 2005, PASP, 117, 1113
Sanders, D. B., et al. 2007, ApJS, 172, 86
Schinnerer, E., et al. 2007, ApJS, 172, 46
Schlegel, D. J., Finkbeiner, D. P., & Davis, M. 1998, ApJ, 500, 525
Scoville, N., et al. 2007, ApJS, 172, 38
Stansberry, J. A., et al. 2007, PASP, 119, 1038